

Near-infrared and Optical Continuum Emission Region Size Measurements in the Gravitationally lensed Quasars Q0957+561 and SBS0909+532

Matthew A. Cornachione 1 Christopher W. Morgan 1 Hayden R. Burger 1, Vyacheslav N. Shalyapin 2,3,4 , Luis J. Goicoechea 2 D, Frederick J. Vrba 5, Scott E. Dahm 5 , and Trudy M. Tilleman 5 Department of Physics, United States Naval Academy, 572C Holloway Rd., Annapolis, MD 21402, USA; cmorgan@usna.edu O.Ya. Usikov Institute for Radiophysics and Electronics, National Academy of Sciences of Ukraine, 12 Acad. Proscury St., UA-61085 Kharkiv, Ukraine 3 Departamento de Física Moderna, Universidad de Cantabria, Avda. de Los Castros s/n, E-39005 Santander, Spain 4 Institute of Astronomy of V.N. Karazin Kharkiv National University, Svobody Sq. 4, UA-61022 Kharkiv, Ukraine 5 United States Naval Observatory, Flagstaff Station, 10391 West Naval Observatory Rd., Flagstaff, AZ 86005, USA Received 2020 July 8; revised 2020 October 2; accepted 2020 October 15; published 2020 December 7

Abstract

We present a microlensing analysis of updated light curves in three filters, the *g*-band, *r*-band, and *H*-band, for the gravitationally lensed quasars Q0957+561 and SBS0909+532. Both systems display prominent microlensing features which we analyze using our Bayesian Monte Carlo technique to constrain the quasar continuum emission region sizes in each band. We report sizes as half-light radii scaled to a 60° inclination angle. For Q0957+561 we measure $\log(r_{1/2}/\text{cm}) = 16.54^{+0.33}_{-0.33}$, $16.66^{+0.37}_{-0.62}$, and $17.37^{+0.49}_{-0.40}$ in g-, r-, and H-band, respectively. For SBS0909 +532 we measure $\log(r_{1/2}/\text{cm}) = 15.83^{+0.33}_{-0.33}$, $16.21^{+0.37}_{-0.62}$, and $17.90^{+0.61}_{-0.63}$ in the g-, r-, and H-band respectively. With size measurements in three bands spanning the quasar rest frame ultraviolet to optical, we can place constraints on the scaling of accretion disk size with wavelength, $r \propto \lambda^{1/\beta}$. In a joint analysis of both systems we find a slope shallower than that predicted by thin disk theory, $\beta = 0.35^{+0.16}_{-0.08}$, consistent with other constraints from multi-epoch microlensing studies.

Unified Astronomy Thesaurus concepts: Quasar microlensing (1318); Gravitational lensing (670); Gravitational microlensing (672); Quasars (1319)

Supporting material: machine-readable tables

1. Introduction

Quasars are difficult objects to study because their small physical sizes limit direct imaging and their immensely broad spectral energy distributions complicate theoretical modeling (Blaes 2007; Antonucci 2013). However, they play a valuable role in shaping our understanding of the universe. Their high luminosity enables observation at a very high redshift, giving us insight into the state of the early universe and galaxy formation (Boyle & Terlevich 1998; Di Matteo et al. 2005). Furthermore, the strong-gravity environments at their centers provide a grounds for stringent testing of general relativity and alternate theories of gravitation (e.g., Fabian et al. 2000; Chartas et al. 2017; Dai et al. 2019). Quasars also have been used to measure the Hubble Constant (e.g., Suyu et al. 2013; Bonvin et al. 2017; Birrer et al. 2019; Chen et al. 2019; Shajib et al. 2019; Wong et al. 2020) and hold promise to be used as standard candles to constrain high-redshift cosmology (Watson et al. 2011; Lusso & Risaliti 2017). To fully unlock the potential of quasars, we must continue to refine our ability to measure their structure.

Multi-epoch quasar microlensing has emerged as one of the best means to measure the size of the quasar continuum emission region in gravitationally lensed quasars (Chang & Refsdal 1979; Kochanek 2004). The flux in lensed quasar images is significantly magnified not only by the smooth mass profile of the lens galaxy, but also by individual lens galaxy stars. This microlensing magnification varies, on timescales of years to decades, as the quasar moves relative to the lensing stars along our line of sight. From a careful analysis of multi-season light curves we can place constraints on the compact quasar continuum emission region size (Kochanek 2004; Kochanek et al. 2006; Pooley et al. 2007;

Eigenbrod et al. 2008; Poindexter et al. 2008; Morgan et al. 2010, 2018; Hainline et al. 2012, 2013; MacLeod et al. 2015; Cornachione et al. 2020). Microlensing measurements agree well with continuum emission region sizes measured through reverberation mapping (Peterson et al. 2004; Bentz et al. 2010; McHardy et al. 2014; Edelson et al. 2015, 2019; Jiang et al. 2016; Cackett et al. 2018), but are anywhere from 2–4 times larger than sizes predicted from flux measurements when adopting the thin accretion disk model of Shakura & Sunyaev (1973).

In a complementary technique, single-epoch microlensing measures quasar sizes from simultaneous observations across multiple bands or from quasar spectra (Bate et al. 2008, 2018; Floyd et al. 2009; Blackburne et al. 2011; Mediavilla et al. 2011; Jiménez-Vicente et al. 2012; Motta et al. 2012, 2017; Rojas et al. 2014, 2020). Although the single-epoch method is sensitive to the unknown mean microlens mass, these sizes agree well with multi-epoch measurements and require significantly less observing time. One additional strength of the single-epoch method is that these multiple band observations provide estimates of microlensing-induced chromatic variability. Chromatic variability allows constraints on the scaling of the quasar size with wavelength, $r \propto \lambda^{1/\beta}$. The parameter β characterizes the effective temperature profile slope of the underlying disk emission. Constraining β may provide crucial insight into the physics governing quasar continuum emission and help distinguish between the many proposed accretion disk models (Cornachione & Morgan 2020).

Unfortunately not all chromatic microlensing measurements agree on the temperature profile slope. While the standard Shakura & Sunyaev (1973) thin disk model predicts $\beta=3/4$, some studies find a shallower slope of $\beta\approx0.5$ (Rojas et al. 2014;

Bate et al. 2018) while others find a steeper slope of $\beta \approx 1.25$ (Motta et al. 2012; Jiménez-Vicente et al. 2014; Rojas et al. 2020). Alternate means to measure the temperature profile slope through reverberation mapping (Cackett et al. 2007, 2018; Jiang et al. 2016; Edelson et al. 2019) do not yet tightly constrain the temperature profile slope, though their findings are generally consistent with the thin disk value. Measurements from the quasar continuum spectral slope support a shallower value of $\beta \geqslant 0.57$ although the precise value depends on the host galaxy dust extinction (Davis et al. 2007; Bonning et al. 2013; Xie et al. 2016).

Multi-epoch chromatic microlensing measurements may be able to better determine the temperature profile slope since the underlying size measurements are more robust to uncertainty in the mean microlens mass. However, because of the intensive observing requirements, most multi-epoch studies have focused on a single observing band. Thus, chromatic microlensing light curves have not been widely employed to estimate the temperature slope. Several studies have analyzed multi-band light curves in the Einstein Cross (Q2237+0305) yielding estimates ranging from $\beta = 0.75$ to $\beta = 1.1$, consistent with the thin disk or mildly steeper (Eigenbrod et al. 2008; Muñoz et al. 2016; Goicoechea et al. 2020). Poindexter et al. (2008) analyzed HE1104-1805 in multiple bands, measuring $\beta = 0.61^{+0.21}_{-0.17}$, also consistent with the thin disk. Two band measurements in SBS 0909+532 and SDSS J0924+0219 yielded a shallower slope of $\beta \approx 0.5$ but the error bars were too broad to exclude other models (Hainline et al. 2013; MacLeod et al. 2015). An alternate method of estimating β from aggregated multi-epoch size measurements at $\lambda \approx 2500 \,\text{Å}$ strongly supported a shallower slope of β < 0.56, but these findings were model dependent (Cornachione & Morgan 2020).

We present here multi-epoch microlensing measurements of three bands, the g-, r-, and H-band, for two gravitationally lensed quasars Q0957+561 (hereafter Q0957) and SBS 0909 +532 (hereafter SBS0909). Q0957 has a particularly long history, starting with its discovery (Walsh et al. 1979) and early microlensing constraints published two decades ago (Refsdal et al. 2000). Both systems are doubly imaged quasars with previous size measurements in the r-band with multi-epoch microlensing (Hainline et al. 2012, 2013). SBS0909 also has a g-band size measurement (Hainline et al. 2013), though the uncertainties were broad. Both quasars have also been analyzed in single-epoch studies, enabling a ready comparison of the results (Mediavilla et al. 2011; Motta et al. 2012; Jiménez-Vicente et al. 2014). We add the longest H-band light curves published for any lensed quasar, complemented by extremely long g- and r-band light curves in both systems. This provides a sample of widely-spaced wavelength measurements, allowing us to explore the power of the constraints that can be achieved with multi-epoch chromatic microlensing.

This paper is organized as follows. We present the data from our monitoring campaign at the United States Naval Observatory (USNO) and Liverpool Robotic Telescope (LRT) in Section 2. We describe our modeling, including strong lensing, time delays, and microlensing, in Section 3. In Section 4 we explain our microlensing analysis techniques and we present our size and temperature slope measurements in Section 5. Finally we discuss the implications of these findings in Section 6.

Throughout we adopt a cosmology of $\Omega_M=0.3$, $\Omega_{\Lambda}=0.7$, and $H_0=70~{\rm km~s^{-1}\,Mpc^{-1}}$ (Hinshaw et al. 2009).

2. Data

2.1. Monitoring Campaigns

Our *r*-band observations are extensions of the programs described in Hainline et al. (2012) and Shalyapin et al. (2012) for Q0957, and Hainline et al. (2013) for SBS0909. These combine observations at the USNO, using the 1.55 m Kaj Strand Astrometric Reflector at Flagstaff Station, and the 2.0 m LRT (Steele et al. 2004) with effective wavelengths of 4868 Å and 6165 Å in the *g*- and *r*-band, respectively. For SBS0909 we also include one epoch from the Hiltner 2.4 m telescope at the MDM Observatory and two epochs from the Wisconsin-Indiana-Yale-NOAO (WIYN) 3.5 m telescope as detailed in Hainline et al. (2013).

The USNO r-band observations of Q0957 from 2008 to 2011 were previously published in Hainline et al. (2012). The LRT r-band curves from 2005 January through 2016 May have also been previously reported (Shalyapin et al. 2008, 2012; Hainline et al. 2012; Gil-Merino et al. 2018). In addition, Hainline et al. (2012) and Gil-Merino et al. (2018) included photometry from the Instituto de Astrofisica de Canarias' (IAC) Teide Observatory from 1996 to 2005. We extend these curves with 48 new nights from the USNO spanning 2011 November through 2017 April. These are collected with three 300 s subexposures per night using either the Tek2K CCD or the EEV CCD with pixel scales of 0."33 and 0."18 respectively. We also present 76 new nights from the LRT using the IO:O camera, with a pixel scale of 0."30, from 2016 October to 2020 January collected with a typical cadence of one 300 s exposure every week. Combining all of these observations we have an exceptional r-band light curve with 1248 epochs spanning twenty-four years, the latter part of which is shown in Figure 1.

For SBS0909 the *r*-band analysis of Hainline et al. (2013) used the USNO observations from 2008 to 2012 and LRT observations from 2005 to 2007 (Goicoechea et al. 2008) and 2010 to 2012. Gil-Merino et al. (2018) published all LRT SBS0909 light curves through 2016 May. We add an additional 44 nights from the USNO, with three 300 s subexposures per night, covering 2012 February through 2017 April, again using either the Tek2K CCD or the EEV CCD. For the updated LRT observations, we present 81 nights from 2016 November through 2020 January. These used the IO:O camera with a typical cadence of one 150 s exposure every week. Altogether we have a combined *r*-band light curve with 510 epochs spanning 16 years, shown in Figure 2.

We include g-band observations of both targets collected from the LRT. For Q0957 the LRT g-band light curve from 2005 January through 2010 June was previously published in Shalyapin et al. (2008, 2012). We present 198 new nights from 2010 December to 2020 January. Before 2012 May these were collected with a single 120 s exposure using the RATCam while later nights used one 150 s exposure with the IO:O camera. These exposures were concurrent with the recent rband observations, and collected at a similar cadence of one observation every 7 days. The total 555 epoch light curve is shown in Figure 1. For SBS0909 the LRT g-band light curve between 2005 and 2007 was previously analyzed in Hainline et al. (2013). In this work we add 195 nights of LRT g-band observations from 2012 October to 2020 February. All exposures were collected with the IO:O camera at a weekly cadence with a single exposure per night of 350 s in the first

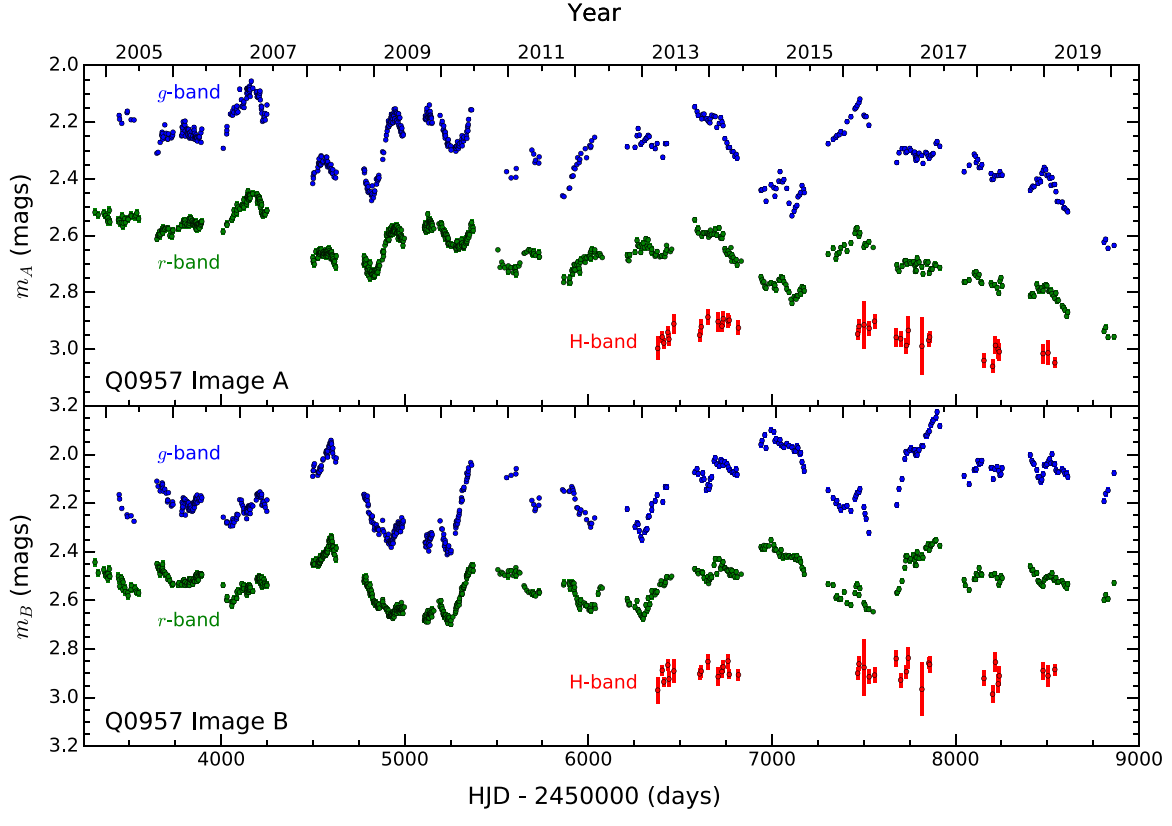


Figure 1. Combined USNO and LRT light curves for Q0957. Top: Image A light curves for the g-band (blue), r-band (green), and H-band (red). Bottom: Image B light curves for the g-band (blue), r-band (green), and H-band (red). The full r-band light curves are not shown and extend back to HJD-2450000 = 117. Light curves are vertically offset for clarity.

2012–2013 season and 300 s thereafter. Our updated SBS0909 *g*-band light curve spans 238 epochs, shown in Figure 2.

Finally, we include *H*-band light curves for both Q0957 and SBS0909. All *H*-band exposures were collected at the USNO with the ASTROCAM (Fischer et al. 2003), a 1024 × 1024 pixel InSb detector with a pixel scale of 0."366 and 10."0 dithering between subexposures. For Q0957 we present 35 nights, with three 400 s subexposures per night, from 2013 March to 2014 June and 2016 March to 2019 February. For SBS0909 we observed 36 nights, with three 440 s subexposures per night, across the same date ranges, 2013 March to 2014 June and 2016 March to 2019 February. Both quasars were monitored at the cadence of roughly one observation per month and a median seeing of 1."0. The *H*-band light curves are included in Figures 1 and 2.

2.2. Data Reduction

Details of the USNO r-band data reduction pipeline are described for Q0957 and SBS0909 in Hainline et al. (2012, 2013). In short, we stack the subexposures from each night to form a combined image. We determine the point-spread function (PSF) and flux normalization in each combined image using nearby reference stars (five stars for Q0957 and three stars for SBS0909). Using the lens galaxy model and astrometry from Lehár et al. (2000) we measure the individual image A and B flux at each epoch, holding the galaxy flux constant over all epochs. For Q0957 we apply a small color offset of $\Delta m_{\rm Tek2K-EEV} = 0.048 \pm 0.002$ mag between the two cameras, using $m_{\rm Tek2K}$ as the reference magnitude, following the findings of Hainline et al. (2012).

The LRT reduction pipeline for Q0957 and SBS0909 is described in detail in Gil-Merino et al. (2018). This is qualitatively similar to the USNO reduction though with a single nightly exposure no stacking was necessary. Once again, we use a nearby reference star to determine the PSF for the exposure and the same star to calculate the flux normalization. Using Hubble Space Telescope astrometry (Lehár et al. 2000), we fit for an image centroid, background, and image fluxes with the IMFITFITS software (McLeod et al. 1998; Lehár et al. 2000). For Q0957 we included a contribution from the lens galaxy, held constant over all epochs, though for SBS0909 the lens galaxy was too faint in these bands to contribute significant flux.

We join the *r*-band USNO and LRT light curves using an offset of 14.43 mag in Q0957 and 14.10 mag in SBS0909, consistent with the offsets found in Hainline et al. (2012, 2013). A sample of the *g*- and *r*-band curves are given in Tables 1–4 and these curves are provided in their entirety in electronic format. We also bin the light curves, which reduces the run time of the microlensing analysis code. We choose a binning of 20 days for the long Q0957 *r*-band curve and 7 days for the SBS0909 *r*-band curve and both *g*-band curves. The microlensing variability is on a much longer timescale than our binning windows so this has a negligible influence on the size measurements.

For our *H*-band light curves we modify our data reduction pipeline to better account for the high sky background, brighter lens galaxy, and increased incidence of detector defects. We process each subexposure, first modeling the sky background as a smoothly varying shape with twelfth order Legendre polynomials along both pixel columns and rows, masking all

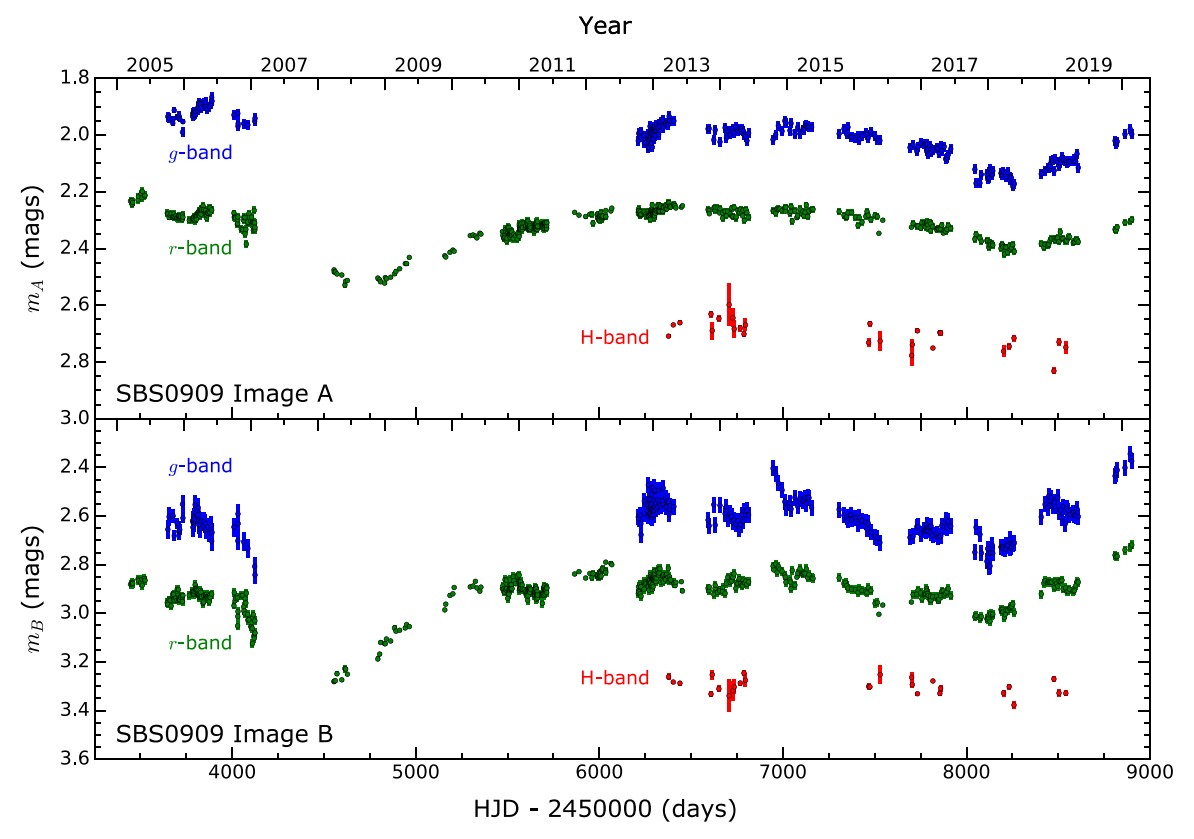


Figure 2. Combined USNO and LRT light curves for SBS0909. Top: Image A light curves for the *g*-band (blue), *r*-band (green), and *H*-band (red). Bottom: Image B light curves for the *g*-band (blue), *r*-band (green), and *H*-band (red). Light curves are vertically offset for clarity.

 Table 1

 Q0957 Combined r-band Light Curve from Teide Observatory, LRT, and USNO

HJD- 2450000 (days)	Image A (mag)	Error A (mag)	Image B (mag)	Error B (mag)	Observatory
117.0000 118.0200 119.0600 120.0400 122.0000	2.532 2.523 2.537 2.486 2.574	0.0230 0.0230 0.0230 0.0230 0.0220 0.0230	2.480 2.472 2.487 2.432 2.514	0.022 0.022 0.022 0.021 0.022	teide teide teide teide teide

(This table is available in its entirety in machine-readable form.)

Table 2
Q0957 g-band Light Curve from the LRT

HJD- 2450000 (days)	Image A (mag)	Error A (mag)	Image B (mag)	Error B (mag)
3443.912	2.671	0.007	2.604	0.008
3445.893	2.684	0.007	2.622	0.008
3457.931	2.699	0.007	2.661	0.007
3486.876	2.661	0.007	2.687	0.007
3488.876	2.656	0.007	2.695	0.007

(This table is available in its entirety in machine-readable form.)

stars, cosmic rays (astroscrappy, 6 van Dokkum 2001), and detector defects. We subtract this smooth term and then flat-field the image.

		una	35110		
HJD- 2450000	Image	Error A	Image	Error	
(days)	A (mag)	(mag)	B (mag)	B (mag)	Observatory
3038.664	2.303	0.009	2.899	0.013	mdm
3048.620	2.283	0.007	2.910	0.007	wiyn
3153.652	2.272	0.007	2.964	0.008	wiyn
3445.888	2.233	0.014	2.881	0.018	lrt
3452.928	2.232	0.014	2.880	0.018	lrt

(This table is available in its entirety in machine-readable form.)

Table 4 SBS0909 *g*-band Light Curve from the LRT

HJD-	Image	Error	Image	Error
2450000 (days)	A (mag)	A (mag)	B (mag)	B (mag)
3649.208	2.502	0.017	3.553	0.038
3656.220	2.508	0.017	3.501	0.038
3676.166	2.525	0.010	3.498	0.022
3677.165	2.512	0.012	3.497	0.027
3684.174	2.480	0.010	3.579	0.022

(This table is available in its entirety in machine-readable form.)

Instead of stacking the subexposures, we fit for the image A and B fluxes in each individual exposure, still holding the galaxy flux constant across all epochs. We retain the USNO *r*-band reference stars for both Q0957 and SBS0909 and determine the PSF and flux normalization within each

https://zenodo.org/record/1482019

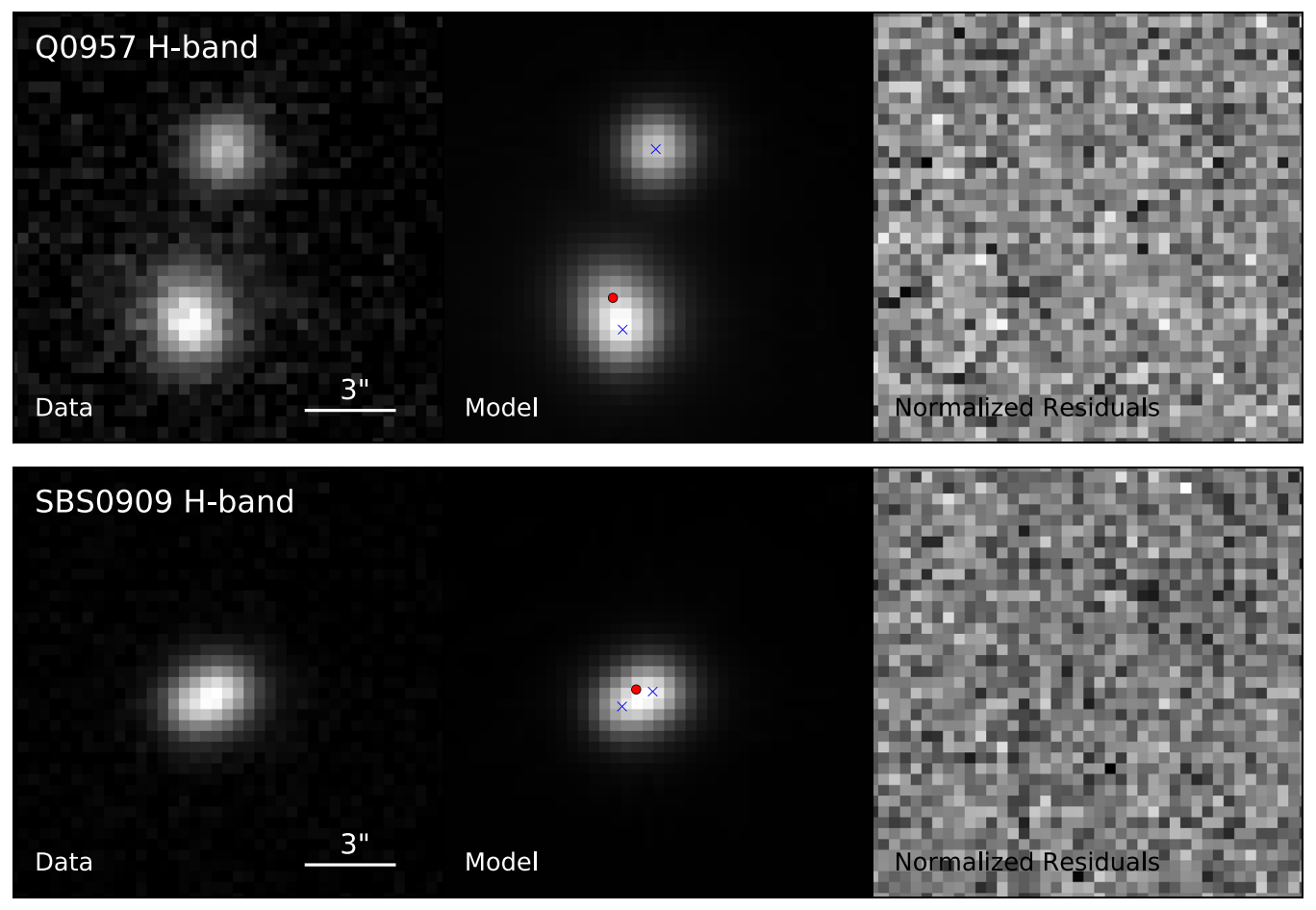


Figure 3. Data (with sky background subtracted), model, and error-normalized residuals for the H-band fits to Q0957 (top) and SBS0909 (bottom) of a typical subexposure from 2016 October 10. In the center panel, the positions of the quasar image centroids are indicated with a blue \times and the galaxy position with a red circle.

subexposure. We again use the astrometry from Lehár et al. (2000) as an initial prediction of the relative quasar positions, but allow the image and galaxy centroids to vary within the measurement errors. Example fits to Q0957 and SBS0909 are shown in Figure 3.

For our final light curves, we calculate the flux each night as the weighted mean of the measured subexposure fluxes. To eliminate bad images, we reject any subexposures with a poor PSF fit to the reference stars ($\chi^2/N_{\rm dof}>1.5$). We calculate the flux error for the night from the weighted mean of the flux errors in each subexposure i using the standard formula $\sigma=\sqrt{\sum_i(1/\sigma_i^2)}$. For some nights we found that the scatter in individual subexposure flux measurements significantly exceeds this error estimate. In these nights, we include additional systematic uncertainty equal to the standard deviation of the subexposure fluxes. This systematic contribution gives us a conservative error estimate in our final light curves. The final curves are given in Tables 5 and 6.

For Q0957 with an image separation of 6."17, the images are completely deblended, although we still apply a seeing cut of 1."3 because of blending between image B and the lens galaxy. This eliminates 11 of the 103 total subexposures, although we retain at least one good subexposure for each night. In SBS0909 the image A and B separation is only 1."17, requiring a more stringent seeing cut of 0."9 to exclude subexposures with significant flux sharing between images. In total we cut 65

of the 103 subexposures, yielding 19 nights with at least one good subexposure.

3. Modeling

Microlensing analysis of gravitationally lensed quasars requires knowledge of the lens galaxy mass profile, the intrinsic quasar flux variability, and the magnification of stars in the lens galaxy. Here we describe our approach to modeling each of these components.

3.1. Strong Lensing Models

We adopt the same strong gravitational lensing models used in Hainline et al. (2012; Q0957) and Hainline et al. (2013; SBS0909). In both systems we explore a sequence of models with a combination of external shear, a DeVaucouleurs baryonic matter profile, and a Navarro, Frenk, and White (Navarro et al. 1997) dark matter profile. We parameterize this sequence with $f_{M/L}$ ranging from 0.1 to 1.0, where $f_{M/L}$ characterizes the magnitude of the DeVaucouleurs moment relative to a baryonic matter only model. This model sequence allows us to analyze a range of stellar matter convergence to total convergence ratios, κ_*/κ and shear, γ , values which Schechter & Wambsganss (2002) show strongly affects the microlensing statistics.

For Q0957 our model sequence is based on the strong lensing models of Fadely et al. (2010). In SBS0909, as

Table 5Q0957 *H*-band Light Curve from the USNO

Table 6SBS0909 *H*-band Light Curve from the USNO

HJD-2450000 (days)	Image A (mag)	Image B (mag)	Seeing (arcsec)	HJD-2450000 (days
6377.694	3.000 ± 0.042	3.073 ± 0.058	0.76	6352.728
6402.747	2.961 ± 0.021	2.988 ± 0.022	0.98	6376.622
6410.732	2.981 ± 0.019	3.046 ± 0.020	0.76	6402.701
6432.705	2.947 ± 0.020	2.977 ± 0.025	1.19	6432.652
6438.696	2.970 ± 0.021	3.018 ± 0.024	0.94	6438.648
6465.656	2.914 ± 0.034	2.992 ± 0.037	1.14	6607.991
6605.976	2.953 ± 0.023	3.010 ± 0.025	0.72	6614.967
6615.012	2.922 ± 0.026	2.988 ± 0.023	0.97	6651.010
6651.046	2.891 ± 0.027	2.959 ± 0.024	0.89	6706.803
6706.856	2.904 ± 0.034	3.004 ± 0.038	0.88	6727.690
6727.745	2.925 ± 0.018	2.993 ± 0.022	0.98	6734.655
6734.712	2.893 ± 0.029	2.970 ± 0.025	1.13	6760.635
6760.693	2.904 ± 0.026	2.953 ± 0.030	1.11	6767.696
6767.738	2.898 ± 0.019	3.001 ± 0.019	0.79	6787.685
6817.652	2.928 ± 0.025	3.015 ± 0.025	0.89	6795.637
7466.747	2.952 ± 0.019	3.001 ± 0.022	0.82	6816.654
7473.878	2.923 ± 0.024	2.966 ± 0.029	1.13	7466.699
7501.765	2.919 ± 0.083	2.988 ± 0.117	1.26	7473.770
7529.708	2.930 ± 0.025	3.015 ± 0.030	1.00	7501.719
7558.653	2.908 ± 0.025	3.015 ± 0.036	1.00	7529.664
7677.013	2.962 ± 0.032	2.950 ± 0.033	1.48	7676.970
7701.018	2.966 ± 0.027	3.016 ± 0.030	1.14	7700.975
7732.923	2.981 ± 0.030	2.982 ± 0.024	0.85	7704.920
7742.909	2.938 ± 0.051	2.945 ± 0.043	1.47	7732.882
7816.920	2.992 ± 0.101	3.042 ± 0.106	0.90	7742.862
7853.792	2.973 ± 0.024	2.961 ± 0.025	1.07	7816.869
7858.814	2.959 ± 0.020	2.958 ± 0.026	0.83	7854.723
8154.874	3.042 ± 0.026	3.003 ± 0.027	0.83	7858.766
8201.764	3.060 ± 0.021	3.047 ± 0.032	0.82	8201.689
8217.764	2.991 ± 0.030	2.959 ± 0.040	1.32	8217.712
8232.774	3.005 ± 0.035	3.055 ± 0.037	0.77	8232.735
8238.743	3.013 ± 0.030	2.988 ± 0.031	1.14	8238.697
8476.875	3.022 ± 0.033	2.993 ± 0.027	1.17	8258.665
8503.994	3.017 ± 0.043	3.008 ± 0.044	0.88	8475.977
8540.861	3.051 ± 0.019	2.994 ± 0.024	0.89	8503.947
				8540 808

HJD-2450000 (days)	Image A (mag)	Image B (mag)	Seeing (arcsec)
6352.728	2.254 ± 0.222	1.457 ± 0.091	1.58
6376.622	1.725 ± 0.007	1.854 ± 0.030	0.70
6402.701	1.710 ± 0.004	1.849 ± 0.004	0.86
6432.652	1.707 ± 0.015	1.846 ± 0.013	1.13
6438.648	1.707 ± 0.008	1.848 ± 0.012	0.90
6607.991	1.677 ± 0.016	1.905 ± 0.031	0.99
6614.967	1.692 ± 0.014	1.866 ± 0.028	0.98
6651.010	1.711 ± 0.010	1.866 ± 0.010	0.86
6706.803	1.748 ± 0.030	1.789 ± 0.024	0.98
6727.690	1.726 ± 0.009	1.832 ± 0.008	0.97
6734.655	1.711 ± 0.023	1.881 ± 0.031	0.93
6760.635	1.564 ± 0.013	2.059 ± 0.022	1.30
6767.696	1.714 ± 0.009	1.857 ± 0.011	0.80
6787.685	1.738 ± 0.013	1.815 ± 0.011	0.81
6795.637	1.709 ± 0.020	1.845 ± 0.024	0.85
6816.654	1.711 ± 0.017	1.847 ± 0.015	1.16
7466.699	1.749 ± 0.006	1.844 ± 0.006	0.79
7473.770	1.743 ± 0.012	1.843 ± 0.007	0.92
7501.719	1.748 ± 0.014	1.877 ± 0.014	1.07
7529.664	1.725 ± 0.011	1.845 ± 0.012	0.99
7676.970	1.672 ± 0.018	1.971 ± 0.019	1.31
7700.975	1.795 ± 0.019	1.832 ± 0.023	1.03
7704.920	1.762 ± 0.019	1.865 ± 0.013	0.79
7732.882	1.726 ± 0.012	1.906 ± 0.013	0.95
7742.862	2.532 ± 0.210	1.439 ± 0.081	1.44
7816.869	1.724 ± 0.011	1.894 ± 0.011	1.03
7854.723	1.746 ± 0.010	1.882 ± 0.012	0.90
7858.766	1.734 ± 0.009	1.876 ± 0.010	0.81
8201.689	1.808 ± 0.018	1.896 ± 0.014	0.88
8217.712	1.911 ± 0.041	1.798 ± 0.036	1.47
8232.735	1.780 ± 0.010	1.874 ± 0.013	0.86
8238.697	1.764 ± 0.015	1.906 ± 0.018	1.09
8258.665	1.777 ± 0.015	1.911 ± 0.013	0.92
8475.977	1.848 ± 0.016	1.851 ± 0.016	1.00
8503.947	1.796 ± 0.021	1.882 ± 0.014	0.91
8540.808	1.791 ± 0.014	1.885 ± 0.010	0.87

explained in Hainline et al. (2013), strong lens modeling is complicated because the lens galaxy models of Lehár et al. (2000) and Sluse et al. (2012) are formally inconsistent. Hainline et al. (2013) explored microlensing statistics under both models and found that microlensing size measurements were not strongly affected by this uncertainty, although the Sluse et al. (2012) models are harder to reconcile with the measured time delay. We follow Hainline et al. (2013) and adopt a blended model in our analysis, using the image and galaxy positions from Lehár et al. (2000) and the lens galaxy shape from Sluse et al. (2012). This blended model best matches the measured time delay and, in our model sequence, covers a wide range of possible stellar convergence values.

3.2. Intrinsic Flux

Before running our analysis we must distinguish the intrinsic quasar variability from the extrinsic microlensing variability. When the time delay between images A and B is known we can eliminate the common intrinsic variability by shifting the light curves to a common time basis and taking the ratio (or the magnitude difference). Fortunately both systems have tightly constrained time delays from their long light curves, allowing us to readily find the difference light curves.

We adopt the time delay of $t_{AB} = 420 \pm 2$ days (A leads B) from Shalyapin et al. (2012) for Q0957 in the r-band. This time delay is very precisely measured due to the high intrinsic variability during the observation period. We confirm that the full, binned g-band light curve is consistent with this time delay using PyCS (Tewes et al. 2013). We shift the curves by the time delay, using the leading image A as the reference curve, and linearly interpolate between nights. For the Q0957 H-band measurements, given the large time delay and an observing gap between 2014 June and 2016 March, we are left with only five well-constrained nights in the difference light curve. To maximize constraints for the microlensing analysis, we include extrapolated dates up to the system time delay on the end of the light curve and interpolated points in the observing gap. For both the interpolated and extrapolated points, we adopt conservative error estimates based on the intrinsic quasar variability. We model this variability using celerite (Foreman-Mackey et al. 2017) to generate a damped random walk based on the observed power spectrum.

For SBS0909 we adopt the time delay of $t_{AB} = -50^{+2}_{-4}$ days (B leads A) from Hainline et al. (2013), formally consistent with the delay of -49 ± 6 days found in Goicoechea et al. (2008). While Eulaers & Magain (2011) found that the time delay of SBS0909 was weakly constrained, we used PyCS to

analyze the longer r-band light curve and found a time delay of -51 ± 6 days, consistent with Goicoechea et al. (2008) and Hainline et al. (2013). As with Q0957, we shift the light curves by the time delay, using the leading image B as the reference curve, and linearly interpolate between nights.

3.3. Microlensing Magnification Patterns

Lens galaxy stars form a complex magnification pattern which we cannot observe directly but can model statistically based on the properties of the lens galaxy. Our microlensing patterns are described in Hainline et al. (2012, 2013). These patterns use the values for stellar convergence κ_* , total convergence κ , and shear γ produced by the lens model sequences described in Section 3.1. These sets include $40 \times 10 = 400$ possible magnification patterns, formed from forty separate trials each using the range of 10 different $f_{M/L}$ values. This samples a wide range of stellar lensing statistics

Within each pattern, we include a range of stellar masses following $dN/dM \propto M^{-1.3}$ with a ratio of maximum to minimum mass of 50 following Gould (2000). The mean stellar microlens mass $\langle M_*/M_{\odot} \rangle$ is left as a free parameter, determined during the microlensing analysis. While the Salpeter mass function is a more common choice, we follow Poindexter & Kochanek (2010) in choosing the bulge mass function of Gould (2000), which we expect to dominate near the galactic center region most relevant to strong lensing. Congdon et al. (2007) found that the microlensing magnification statistics are insensitive to the slope of the mass function and depend more on the dynamic mass range, where our range of 50 is comparable to the broadest range they examined. Thus changes in the stellar mass function are unlikely to have a significant impact on the measured microlensing sizes. These patterns are cast on a 8192 × 8192 pixel grid. We scale these to give a minimum size resolution at one pixel of $0.005R_{\rm E}$ and a maximum size resolution of $40R_{\rm E}$. The Einstein size unit, $R_{\rm E} = D_{\rm OS} \theta_{\rm E}$, is the product of the source (quasar) angular diameter distance and the Einstein radius and scales with the mean microlens mass as $\theta_{\rm E} \propto \langle M_*/M_{\odot} \rangle^{1/2}$. This wide dynamic range is important to obtain simultaneous size constraints in three different bands, where quasar continuum emission region sizes can vary by more than an order of magnitude.

4. Microlensing Analysis

Our microlensing analysis follows the method detailed in Kochanek (2004) and used in the previous studies of Q0957 (Hainline et al. 2012) and SBS0909 (Hainline et al. 2013). We run single band analyses on the *r*- and *g*-band difference light curves. For the *H*-band we run a joint size analysis with the long *r*-band curves. We also run a joint analysis combining the *r*- and *g*-bands to check for consistency with the single band findings.

4.1. Single Band Analysis

The quasar continuum flux magnification varies as the quasar moves across the screen of stellar lenses relative to our line of sight. To analyze this variability, we first convolve each magnification pattern with a Gaussian kernel representing the quasar shape. Our analysis uses a Gaussian convolution kernel for simplicity and speed of calculation because Mortonson et al. (2005) showed that the measured microlensing half-light sizes are weakly sensitive to the source shape, a conclusion supported in

other studies (Kochanek 2004; Congdon et al. 2007). We explore 21 different scale sizes of the Gaussian kernel, covering Einstein size units of $\log(\hat{r}_s) = [14.5, 18.0] \langle M_*/M_{\odot} \rangle^{1/2}$ cm for Q0957 and $\log(\hat{r}_s) = [14.5, 18.5] \langle M_*/M_{\odot} \rangle^{1/2}$ cm for SBS0909. While the upper limit of $\log(\hat{r}_s)$ in SBS0909 slightly exceeds the size scale of the magnification patterns, we found this does not impact any of our key findings. Our Monte Carlo analysis samples possible trajectories for both image A and B across these convolved patterns. We randomize starting points, (x_i, y_i) , and directions, ϕ , and choose effective source velocities, in Einstein units, from $\hat{v}_e = [10^1, 10^6] \langle M_*/M_{\odot} \rangle^{1/2} \text{ km s}^{-1}$. For the maximal \hat{v}_e , given our long light curves, the trajectories will cross an edge of the finite magnification pattern. Our microlensing code includes periodic boundary conditions to allow for this. We find, however, that both systems favor $\hat{v}_e < 2 \times 10^4 \langle M_*/M_{\odot} \rangle^{1/2} \, \mathrm{km \ s^{-1}}$, so edge effects do not impact our reported measurements of $r_{1/2}$. We then compare these microlensing curves to the time-delay shifted difference curves described in Section 3.2, allowing for source optimization as in Kochanek (2004), and evaluate the quality of fit using the χ^2 metric. The degrees of freedom, N_{dof} , are given by the number of points in the difference curve minus the number of microlensing variables $(x_i, y_i, \phi, \hat{v}_e, \hat{r}_s, \kappa_*/\kappa)$. For Q0957 we add an overall flux ratio uncertainty of 0.1 mag between images A and B. This effectively accounts for errors in the strong lens models, any lens galaxy substructure magnification, differential dust extinction, and microlensing. Because the strong lens models of SBS0909 are less certain (see Section 3.1), we adopt a flux ratio uncertainty of 0.2 mag in this system.

To speed up computational time and reduce output file sizes we impose a χ^2 threshold in each system. We adopted r-band constraints of $\chi^2/N_{\rm dof} \leqslant 2.1$ for Q0957 and $\chi^2/N_{\rm dof} \leqslant 2.4$ for SBS0909 and g-band constraints of $\chi^2/N_{\rm dof} \leqslant 2.1$ for Q0957 and $\chi^2/N_{\rm dof} \leqslant 1.9$ for SBS0909. We select these thresholds by examining the total probability at each $\chi^2/N_{\rm dof}$, which is the product of the number of good fits at a given χ^2 times the probability from Kochanek (2004)

$$P(\chi^2) \propto \Gamma \left[\frac{N_{\text{dof}} - 2}{2}, \frac{\chi^2}{2f_0^2} \right],$$
 (1)

where Γ is the incomplete gamma function and f is a magnitude error scaling factor. We set $f_0 = 1$ as in Kochanek (2004). Solutions with $\chi^2/N_{\rm dof}$ above these thresholds contribute negligible statistical weight ($<\sim$ 0.1%) toward the final solution.

Upon conclusion of the runs, we convert from Einstein units to physical units following Kochanek (2004) and Mosquera & Kochanek (2011). This method uses cosmological models to constrain the physical velocity, v_e , which permits a determination of the mean microlensing mass $\langle M_*/M_\odot \rangle$ from the distribution of effective source velocities, \hat{v}_e . We marginalize over the microlens mass, $f_{M/L}$, and trajectory variables (v_e , ϕ , v_i , v_i) to convert the distribution of Einstein sizes, \hat{r}_s , found in our analysis to a posterior distribution on the physical size of the quasar continuum emission region, r_s .

We perform the Monte Carlo runs across the 400 trial magnification patterns with the United States Naval Academy high performance cluster, TheARC.⁷ The number of runs performed for each system are shown in Table 7 and are sufficiently large such that variations in the number of runs

⁷ https://www.usna.edu/ARCS/index.php

Quasar	Analysis	$N_{ m trials}$	$\chi^2/N_{\rm dof}$ threshold	N_{good}
Q0957	g-band only	4×10^{9}	2.1	1.7×10^{6}
	r-band only	4×10^{10}	2.1	1.3×10^{7}
	r/g-band joint	2.7×10^{8}	1.9	1.2×10^{6}
	r/H-band joint	2.7×10^{8}	1.9	3.1×10^{7}
	g/H-band joint	3.6×10^{7}	2.1	5.0×10^{6}
SBS0909	g-band only	4×10^{9}	2.4	2.6×10^{6}
	r-band only	4×10^{10}	1.9	2.5×10^{5}
	r/g-band joint	5.2×10^{6}	3.0	827
	r/H-band joint	5.2×10^6	3.0	5.1×10^4

have a negligible impact on the measured sizes. The SBS0909 r-band has significantly fewer runs within the χ^2 threshold than Q0957 because of a very high magnitude microlensing event from 2007 to 2010. Though this feature is harder to fit, it provides strong size constraints.

4.2. Two-band Joint Analysis

The H-band light curves are too sparse to return a tight constraint when analyzed alone. Following the procedure used for X-rays (e.g., Morgan et al. 2008; Dai et al. 2010) and short g-band curves (Hainline et al. 2013; MacLeod et al. 2015), we perform a joint optical and H-band analysis. This means we only fit the H-band difference curves to the solutions that satisfy the χ^2 threshold of the r-band runs (see Table 7).

For each good r-band solution, we repeat the analysis described in Section 4.1 at 21 steps in quasar size. We explore the same size range in H-band of $\log(\hat{r}_s) = [14.5, 18.5] \langle M_*/M_\odot \rangle^{1/2}$ cm for SBS0909. For Q0957 we are able to compress this range, retaining all valid solutions, to $\log(\hat{r}_s) = [15.1, 17.75] \langle M_*/M_\odot \rangle^{1/2}$ cm, giving a finer size resolution. In the joint analysis, we use the same trajectories (v_e, ϕ, x_i, y_i) from the good r-band solutions rather than exploring a random set. We assign equal statistical weight to the difference curve fits from each band and use an overall threshold of $\chi^2/N_{\rm dof} \leqslant 1.9$ in Q0957 and $\chi^2/N_{\rm dof} \leqslant 3.0$ in SBS0909. We repeat the Bayesian posterior analysis on the results, also marginalizing over the r-band sizes.

A portion of the *H*-band flux is likely composed of scattered emission or host galaxy stars (Vanden Berk et al. 2001; Glikman et al. 2006; Hernán-Caballero et al. 2016). This large-scale diluting flux is not significantly microlensed. In previous microlensing studies, the measured source size has been found to decrease as flux dilution increases (e.g., Dai et al. 2010). We seek to quantify the impact of this dilution in our joint *H*-band analysis.

Based on the spectral catalog published by Calderone et al. (2017), we estimate that the host galaxy can contribute up to 50% of the total flux around 6800 Å. However Shen (2016) found that host galaxy contamination decreases significantly for high luminosity quasars. Since both Q0957 and SBS0909 have bolometric luminosities of $L_{\rm bol} \approx 10^{46} \, {\rm erg \ s^{-1}}$ (Assef et al. 2011), we expect a much smaller diluting fraction. Indeed we find that if we restrict to Calderone et al. (2017) quasars with $L_{\rm bol} > 10^{45} \, {\rm erg \ s^{-1}}$ we find only 10% host galaxy contamination at 6800 Å. This fraction is roughly consistent with the host galaxy contamination reported in recent near-infrared catalogs (Glikman et al. 2006; Hernán-Caballero et al. 2016). The 6563 Å

 ${\rm H}\alpha$ line can also contribute up to 25% to the total flux in these systems that will not be strongly microlensed. Based on these considerations, we choose to investigate the cases of 20% flux dilution as a typical fraction, and 50% flux dilution as an extreme upper bound.

Although we analyzed the *g*-band light curves independently, we also run a joint *r*- and *g*-band analysis. This provides a check on the findings of the two independent runs and, in principle, the tightest constraints on both sizes. We again explore the same range of $\log(\hat{r}_s)$ and keep all solutions with $\chi^2/N_{\rm dof} \leqslant 3.0$. For Q0957, with a robust *g*-band size measurement, we also computed the sizes under a joint *g*-and *H*-band analysis for comparison.

5. Results

We show the five best-fit difference light curves from the *r*-band analysis and the *H*-band and *g*-band joint analysis in the top panel of Figure 4 for Q0957. Q0957 is undergoing a roughly linear microlensing event continuing nearly a decade since its original report in Hainline et al. (2012), observable both in the *r*- and *g*-band. This places stronger constraints on the sizes than previously reported. The sparse *H*-band difference curve is also plotted.

The Q0957 difference curves, especially in the *g*-band, display features around the 2007, 2009, and 2015 seasons that are related to the sharp variations of image A (see Figure 1) and are not well-fit by the microlensing curves. These features may be evidence of reprocessed broad line emission suggested in Gil-Merino et al. (2018), a hypothesis we plan to investigate in future work. After separately fitting subsections of the Q0957 light curves we find that failure to fit these features has a negligible impact on the microlensing sizes.

For SBS0909 we show the difference curves in the bottom panel of Figure 4. SBS0909 has continued to experience detectable microlensing variability since the size measurements reported in Hainline et al. (2013), better constraining both *r*-and *g*-band sizes. The *H*-band curve in SBS0909 is better sampled than that of Q0957, but shows minimal evidence of microlensing.

5.1. Size Distributions

From our microlensing analysis, we determine posterior distributions for the quasar continuum emission region sizes. These are shown in Figure 5 for Q0957 (left) and SBS0909 (right). In the top panel the solid lines indicate the results from the joint r- and g-band analysis, which are the best-constrained results. The faint dashed lines indicate the single band analysis posterior for both r- and g-bands. For Q0957 the single band findings are consistent with the joint analysis though they favor a slightly larger size. In SBS0909 the r-band size is tightly constrained and does not vary significantly with analysis method. The g-band-only analysis, however, favors a larger continuum emission region size than the joint g-band analysis. This is most likely because the g-band-only difference curve did not cover the significant microlensing event between 2007 and 2010 and fits to this event favor a smaller source size. There are, however, relatively few good fits to the joint r/gband curves (see Table 7), due to the very high microlensing variability in this system.

The bottom panel shows the *r*-band and *H*-band posterior size distributions, with joint constraints indicated with a solid

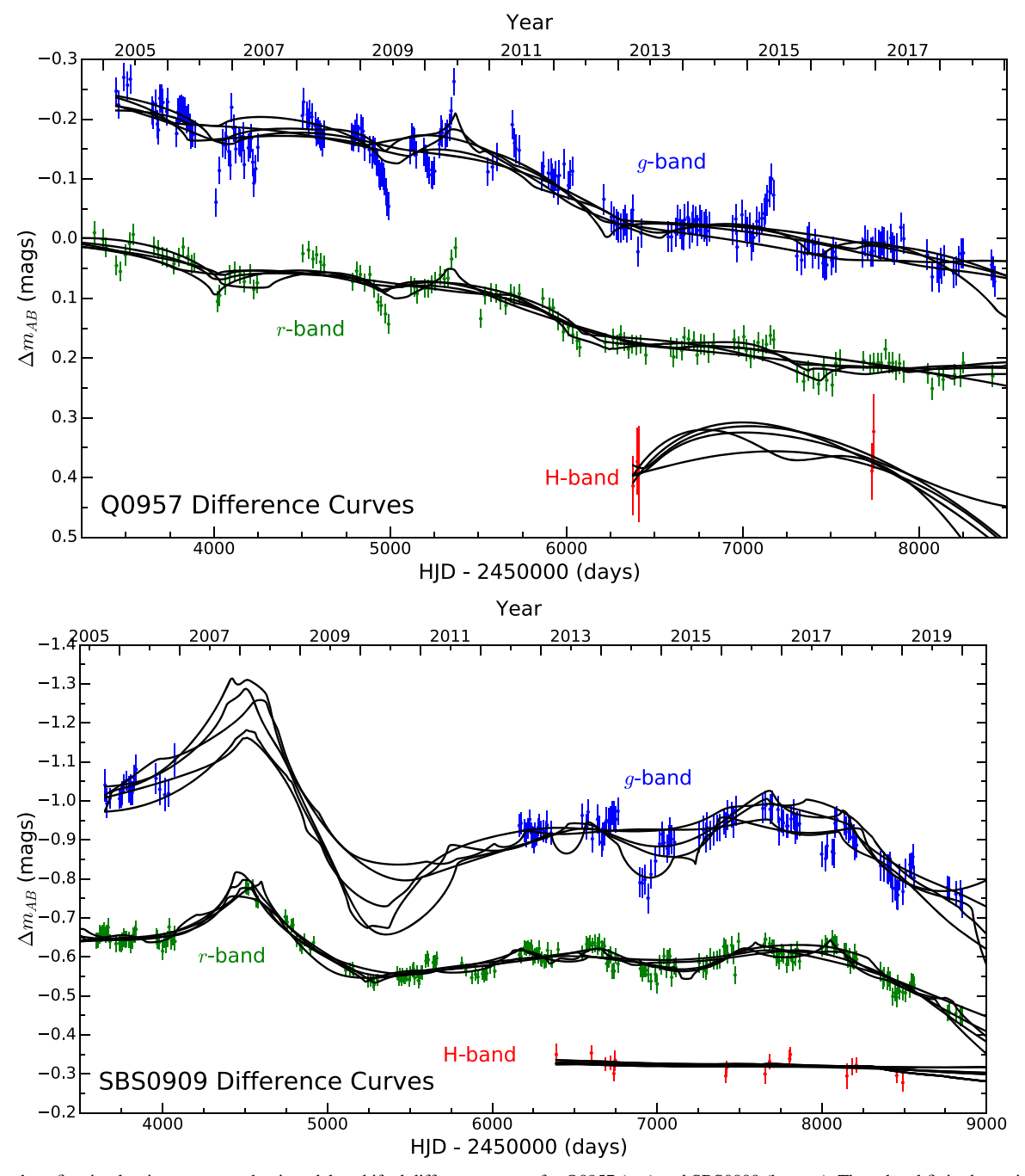


Figure 4. Five best-fit microlensing curves to the time-delay shifted difference curves for Q0957 (top) and SBS0909 (bottom). The g-band fit is shown in blue, the r-band in green, and the H-band in red. For the Q0957 H-band difference we do not show interpolated or extrapolated points with error bars $\geqslant 0.1$, although we do include these points in the joint analysis. All difference light curves are vertically offset for clarity.

line. As in the top panel, the faint dashed green line indicates the r-band-only analysis results and the solid red line indicates the H-band size from the joint r/H-band analysis. The faint dashed red line indicates the H-band size measurements if we assume 20% of the flux is emitted at large (unmicrolensed) scales. As expected from the sparse difference curve, the Q0957 H-band size measurement gives the broadest distribution, favoring a large H-band size. This distribution shifts noticeably as the flux dilution increases. At 20% flux dilution the H-band size estimate decreases by 31%. This size estimate with dilution is similar to the size found when jointly analyzing the g/H-band curves. With 50% flux dilution the H-band size

becomes more comparable to the r-band size. While the 50% dilution case may not be physically likely, this shows that large-scale flux emission can have a significant impact on size measurements. In any case, the H-band sizes under varying dilution factors are formally consistent given the high uncertainty on each measurement.

Despite a longer H-band light curve in SBS0909, we also find a broad distribution. Furthermore, in SBS0909 the distribution of H-band values of \hat{r}_s peaks at the size limit of our magnification patterns, $\approx 18.1 \langle M/M_{\odot} \rangle^{1/2}$ cm. This means that we cannot explore larger sizes and must consider these H-band size measurements a robust lower limit only. The

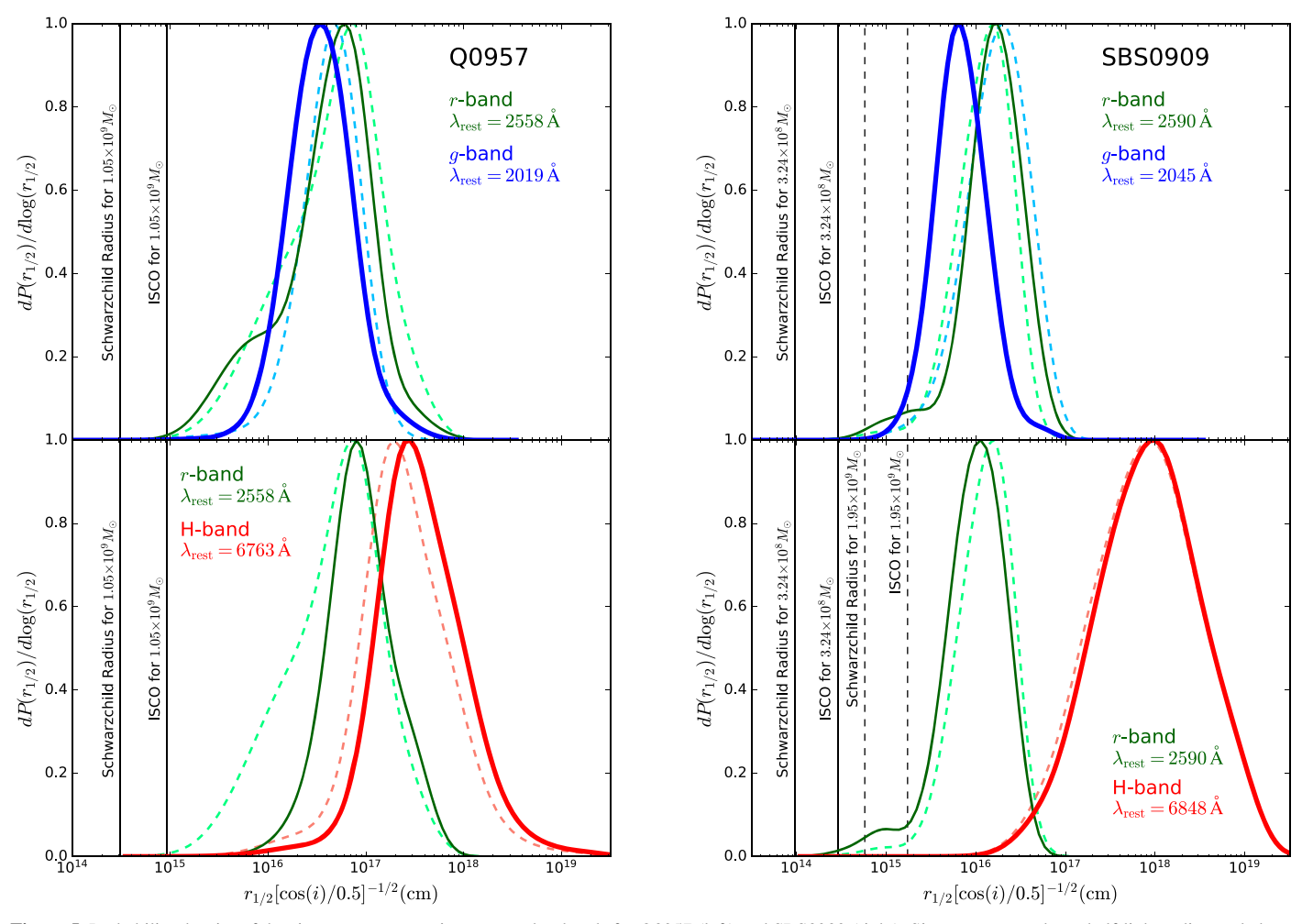


Figure 5. Probability density of the size measurements in r-, g-, and H-bands for Q0957 (left) and SBS0909 (right). Sizes are reported as a half-light radius scaled to a 60° inclination angle. Top: comparison between the r-band (green) and g-band (blue) sizes. The solid lines (g-band is the heavier line) indicate the results of the joint analysis while the faint dashed lines show the independent analysis in each band. Bottom: comparison between the r-band (green) and H-band (red) sizes. The solid green line gives the r-band under the joint analysis while the heavier solid red line gives joint analysis r/H-band results. The faint dashed green line gives the r-band-only result while the faint dashed red line shows the constraint on H-band size if we include 20% large-scale flux dilution. The vertical lines show the Schwarzchild radius and innermost stable circular orbit (ISCO) for the black hole masses found by Assef et al. (2011). For SBS0909 we show lower and upper mass estimates of $10^{8.51} M_{\odot}$ using C IV (solid line) and $10^{9.29} M_{\odot}$ using H β (dashed line).

distribution shifts toward smaller sizes for increasing flux dilution, but not as significantly as for Q0957. Even with 50% flux dilution the H-band lower limit is larger than the r-band size estimate.

All size measurements are reported in Table 8, where the median posterior scale size is cast as a half-light radius, $r_{1/2}$, and scaled to a nominal 60° inclination ($\cos(i) = 0.5$). We indicate the rest-frame wavelengths, based upon the redshifted central wavelengths for each band. The bold results are those we adopt as our reported sizes. These measurements come from our joint analyses, which are the most robustly constrained size measurements. For the *H*-band we adopt the sizes under 20% flux dilution as the most physically likely case.

5.2. Mean Microlens Mass

Microlensing is uniquely poised to uncover information about the statistics of stars in the lens galaxy (Pooley et al. 2019). While we have not optimized our study to investigate lens galaxy stars, we naturally compute a distribution for the mean microlens mass (see Section 4.1). We show these distributions for both Q0957 and SBS0909 in Figure 6.

Because the width of the mass distribution is proportional to the square of the width of the velocity distribution, these constraints are broad. The Q0957 distribution favors relatively small mass stars and is consistent with the $0.52\,M_\odot$ microlens mass found in Q2237 (Poindexter & Kochanek 2010). The SBS0909 distribution allows for a significant contribution from microlenses with low mass, including brown dwarfs and free-floating Jupiters. Though constraints from microlensing in the Milky Way disfavor significant mass in these objects (Mróz et al. 2017), X-ray microlensing of quasars can be interpreted as evidence of an abundance of free-floating planets in lens galaxies (Bhatiani et al. 2019). Degeneracies between the mean microlens mass and the unknown source velocity limit any conclusions we can draw here, but this may be an interesting avenue for further study.

5.3. Size Scaling with Wavelength

We use the sizes reported in Table 8 to estimate the slope β in $r \propto \lambda^{1/\beta}$ using a maximum likelihood fit in log-space to $\log(r_{1/2}) = (1/\beta)\log(\lambda) + C$. We use the distributions shown in Figure 5 as the size priors in each band, using those

Table 8Microlensing Size Measurements

Quasar	Filter	$\log (r_{1/2}[\cos(i)/0.5]^{-1/2} \text{ cm}^{-1})$	$\lambda_{ m rest}$	Analysis Method
Q0957	g	$16.65^{+0.28}_{-0.32}$	2019 Å	g-band only
		$16.54^{+0.33}_{-0.33}$	2019 Å	r/g-band joint
		$16.55^{+0.29}_{-0.31}$	2019 Å	g/H-band joint
	r	$16.73^{+0.42}_{-0.61}$	2558 Å	r-band only
		$16.66^{+0.37}_{-0.62}$	2558 Å	r/g-band joint
		$16.93^{+0.37}_{-0.33}$	2558 Å	r/H-band joint
	Н	$17.53^{+0.48}_{-0.39}$	6763 Å	r/H-band joint
		$17.21^{+0.37}_{-0.35}$	6763 Å	g/H-band joint
		$17.37^{+0.49}_{-0.40}$	6763 Å	r/H-band w/ 20% dilution
		$16.91^{+0.53}_{-0.48}$	6763 Å	r/H-band w/ 50% dilution
SBS0909	g	$16.25^{+0.33}_{-0.38}$	2045 Å	g-band only
		$15.83^{+0.30}_{-0.28}$	2045 Å	r/g-band joint
	r	$16.11^{+0.28}_{-0.34}$	2590 Å	r-band only
		$16.21^{+0.30}_{-0.34}$	2590 Å	r/g-band joint
		$16.00_{-0.36}^{+0.31}$	2590 Å	r/H-band joint
	Н	$17.93^{+0.59}_{-0.61}$	6848 Å	r/H-band joint
		$17.90^{+0.61}_{-0.63}$	6848 Å	r/H-band w/ 20% dilution
		$17.83^{+0.66}_{-0.67}$	6848 Å	r/H-band w/ 50% dilution

Note. Sizes are reported as half-light radii scaled to 60° inclination. Our adopted values from the joint analyses are indicated in bold.

associated with the bold lines in Table 8, and for our wavelength we use the central rest-frame wavelength given in Table 8. We adopt the standard χ^2 metric for our likelihood calculation. We run this analysis in each individual system and in the joint sample, where both quasars have a different constant, C, but the same scaling β .

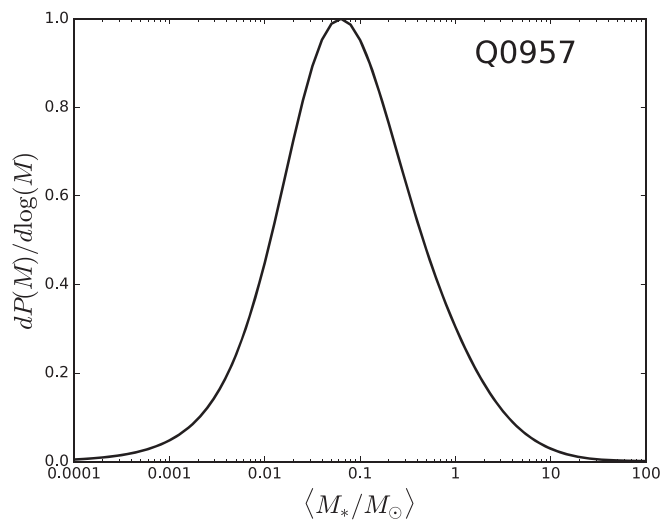
The best-fit curves are shown in Figure 7. In the joint analysis, using the H-band sizes from the r/H-band joint analyses with 20% flux dilution, we find $\beta = 0.35^{+0.16}_{-0.08}$. Analyzing the individual systems separately we find $\beta = 0.54^{+0.58}_{-0.22}$ for Q0957 and $\beta = 0.25^{+0.13}_{-0.06}$ for SBS0909. The slope for Q0957, while formally consistent with the fiducial Shakura & Sunyaev (1973) thin disk value of $\beta = 3/4$, is suggestive of a shallower slope. The slope for SBS0909 is much shallower but even so our joint analysis does not exclude the thin disk model at 2σ $(\beta = 0.35^{+0.54}_{-0.13})$. If we compute β again increasing the *H*-band large-scale flux dilution to 50%, we find a larger joint system value of $\beta=0.42^{+0.25}_{-0.11}$. The individual system values also increase to $\beta=0.63^{+1.33}_{-1.90}$ for Q0957 and $\beta=0.26^{+0.15}_{-0.07}$ for SBS0909. We find a similar value of β when using the distribution for the H-band size from the Q0957 joint g/H-band analysis. We also attempted to fit the joint sample excluding the *H*-band, but the uncertainty in our findings was so high that β was essentially unconstrained.

6. Discussion

For Q0957 our updated r-band size measurement is completely consistent with the findings of Hainline et al. (2012), though our constraints are now much tighter, as expected from a longer light curve with significant microlensing. The reverberation-based size measurement of the r-band source in Q0957 is consistent with our microlensing-based size measurement, although it is close to the lower limit of our 1σ interval (Gil-Merino et al. 2012, 2018). These measurements may show

closer agreement if we include an analysis of broad line emission delays proposed in Gil-Merino et al. (2018). Q0957 has also been studied using the single-epoch microlensing technique. Jiménez-Vicente et al. (2014) analyzed time-delay corrected flux ratios from Motta et al. (2012) to yield size estimates at three wavelengths between 1216 and 2796 Å. To compare to our findings, we converted their Gaussian scale radius to a half-light radius, scaled to our nominal 60° inclination, and computed sizes at the rest-frame wavelengths of each band, giving sizes of $\log(r_{1/2}/\text{cm}[\cos(i)/0.5]^{1/2}) = 16.55$ and 16.58 in the g-band and r-band, respectively, at a nominal $0.3 M_{\odot}$ mean microlens mass. Although their observations did not cover longer wavelengths, their fits predict an H-band size of $\log(r_{1/2}/\text{cm}[\cos(i)/0.5]^{1/2}) = 16.69$. These sizes are consistent with ours within formal statistical errors, although the Jiménez-Vicente et al. (2014) findings suggest less chromatic variability.

In SBS0909 both our r- and g-band sizes are consistent with Hainline et al. (2013), although our reported sizes are larger. This lessens the apparent tension between the Hainline et al. (2013) size measurements and the large ISCO implied by the H β measurement of the central black hole with a mass $10^{9.29} M_{\odot}$ (Assef et al. 2011). Though our microlensing size measurements still disfavor such a large black hole, they are easily reconciled with the C IV mass estimate of $10^{8.51} M_{\odot}$ (Assef et al. 2011). Microlensing signatures in merged spectra from this system were also analyzed by Mediavilla et al. (2011) and re-analyzed (with the same data) by Jiménez-Vicente et al. (2014). In both analyses the wavelength range spans all three of our bands. We again scale the reported results of both studies to half-light radii at 60° inclination, adopt a $0.3 M_{\odot}$ mean microlens mass, and compute the sizes at the rest wavelengths of each of our bands. For Mediavilla et al. (2011) this gives sizes of $\log(r_{1/2}/\text{cm}[\cos(i)/0.5]^{1/2}) = 16.37$, 16.47, and 16.85 in the g-band, r-band, and H-band, respectively. These findings are



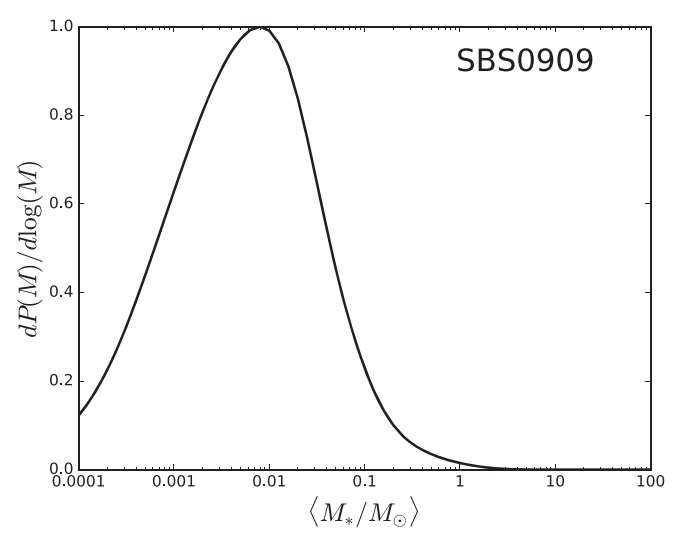


Figure 6. Probability density of the mean microlens mass $\langle M_*/M_{\odot} \rangle$ in Q0957 (left) and SBS0909 (right).

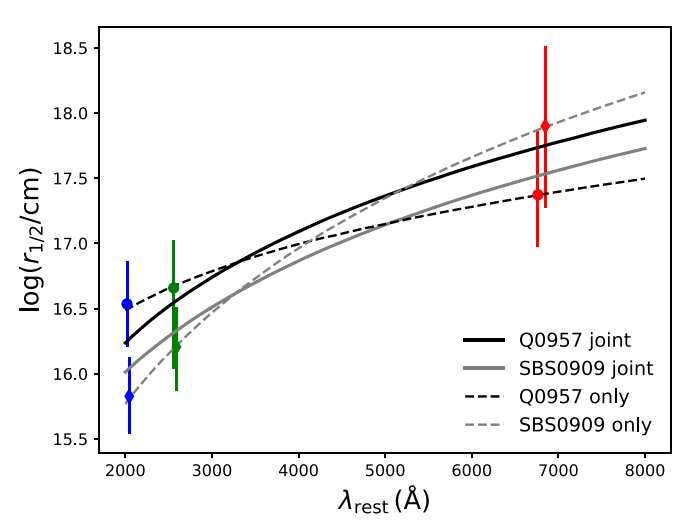


Figure 7. Continuum emission region size scaling with wavelength, $r \propto \lambda^{1/\beta}$. Microlensing size measurements for Q0957 are shown with solid circles and for SBS0909 with solid diamonds. The g-, r-, and H-band sizes are indicated in blue, green, and red, respectively. Best-fit curves are shown for the two systems combined (solid lines) and the dashed lines for the individual systems where Q0957 is black and SBS0909 is gray.

fully consistent with the size estimates from Jiménez-Vicente et al. (2014) of $\log(r_{1/2}/\mathrm{cm}[\cos(i)/0.5]^{1/2})=16.33$, 16.42, and 16.78 in the *g*-band, *r*-band, and *H*-band, respectively. Though formally consistent with our findings, these sizes are systematically larger than our values reported in Table 8. A smaller mean microlens mass, consistent with our distribution shown in Figure 6, would help reconcile these size measurements, though an abundance of such small mass objects in the lens galaxy may be physically unlikely.

As discussed in Cornachione & Morgan (2020), a reliable measurement of the temperature profile slope, β , could help refine physical models of quasar accretion. In this study we found evidence for a shallow profile of $\beta=0.35^{+0.16}_{-0.08}$, with individual estimates of $\beta=0.54^{+0.58}_{-0.22}$ in Q0957 and $\beta=0.25^{+0.13}_{-0.06}$ in SBS0909. In stark contrast, Jiménez-Vicente et al. (2014) found evidence for a steep temperature profiles of $\beta=2.0$ in Q0957 and $\beta=1.3$ in SBS0909. Mediavilla et al. (2011) also found a steeper temperature profile slope of $\beta=1.1$ in SBS0909. Although the

error bars on each individual slope measurement are large, the disagreement is dramatic, particularly when comparing the eight system aggregate value of $\beta=1.25\pm0.2$ (Jiménez-Vicente et al. 2014) to our joint slope of $\beta=0.35^{+0.16}_{-0.08}$, findings which are formally inconsistent. The large difference between these temperature profiles has significant implications for the underlying structure of the quasar continuum emission region.

This disagreement is similar to that found by Cornachione & Morgan (2020) using a model-based approach with aggregated multi-epoch measurements at $\lambda_{\rm rest} \approx 2500\,{\rm Å}$. Both the cause for the contention and the path to a resolution with future measurements are not readily apparent. One potential limitation of single-epoch chromatic microlensing is that in the absence of strong chromatic variation, the single-epoch method may favor an overly steep temperature profile (Bate et al. 2018). The single-epoch flux ratios for Q0957 are based on spectra collected in 1999 and 2000 (Motta et al. 2012), a period during which our difference light curves show no significant microlensing variability. This could explain why Q0957 has such a large and poorly constrained temperature profile slope. From our SBS0909 light curves it is less apparent whether the chromatic variation is low during the observations from Mediavilla et al. (2011), as some of these spectra predate our light curves. The spectrum used in their analysis was, however, a composite of spectra collected over the span of several years so it is possible that intrinsic quasar variability influenced the single-epoch results in this system.

Our measurement for the slope is preliminary and only uses a sample of two quasars. Small changes in size measurements can have a large impact on the slope. For example, the difference between our joint g-band size in SBS0909 and the g-band only analysis (see Table 8) would dramatically change our result. With only 827 good fits, the joint g-band size in SBS0909 is the least robust of all our measurements. Of the two systems in our study, SBS0909 has the shallower slope, which may turn out to be, at least in part, impacted by this uncertainty. Furthermore the H-band light curves likely contain a blend of the compact continuum emission and larger scale emission from host galaxy stars, reprocessed high energy emission, and the $H\alpha$ emission line. When including a diluting flux fraction, we found that H-band sizes decrease, substantially in the case of Q0957, with the percentage of contaminating flux. In Section 5.3, we found that β

steepens when accounting for this dilution. Though our measurements still favor a shallower value of $\beta \approx 0.42$ under 50% flux dilution, this effect lessens the tension between our findings and those of other studies. While we know the Gaussian and thin disk source profiles return consistent sizes (Mortonson et al. 2005), we did not explore whether modeling the source as a thin disk affects the temperature profile slope. This may be an important avenue for future study, though since Mediavilla et al. (2011) and Jiménez-Vicente et al. (2014) both used Gaussian sources, it is unlikely to resolve the discrepancy between studies. Measurements including more wavelengths, particularly those between the r-band and H-band, may give the best constraints on β and allow a better characterization of the underlying quasar continuum emission region structure.

The results here show the utility of multi-epoch microlensing to measure quasar sizes in multiple bands spanning a wide range of quasar rest wavelengths, including H-band ground-based observations. With only two quasars we see emerging evidence of a shallow temperature profile slope. These constraints will be improved dramatically even with a modest sample size. LSST (LSST Science Collaboration et al. 2009) is developing a microlensing monitoring program which will produce multi-epoch light curves in $\mathcal{O}(1000)$ lensed quasars covering several observing bands in this key wavelength range. Microlensing events will be used as triggering for complementary single-epoch microlensing measurements, which well help check for consistency between methods. Combining the technique here with this expansive program may yield tremendous insights into quasar structure in the coming decade.

We thank Christopher Kochanek for the use of his microlensing analysis code. We also thank Bonnie Lucas and the USNA ARC team for their help using TheARC computing cluster.

This material is based upon work supported by the National Science Foundation under grants AST-1614018 and AST-2007680 to M.A.C. and C.W.M.

This paper is partially based on observations made with the Liverpool Telescope, which is operated on the island of La Palma by Liverpool John Moores University in the Spanish Observatorio del Roque de los Muchachos of the Instituto de Astrofisica de Canarias with financial support from the UK Science and Technology Facilities Council. We thank the staff of this robotic telescope for a kind interaction before, during, and after the observations. V.N.S. and L.J.G. have been supported by the MINECO/AEI/FEDER-UE grant AYA2017-89815-P and University of Cantabria funds.

Facilities: USNO:61in, Liverpool:2 m.

Software: Anaconda, PyCS (Tewes et al. 2013), IMFITFITS (McLeod et al. 1998; Lehár et al. 2000), astroscrappy (van Dokkum 2001, https://zenodo.org/record/1482019), celerite (Foreman-Mackey et al. 2017).

ORCID iDs

Matthew A. Cornachione https://orcid.org/0000-0003-1012-4771
Christopher W. Morgan https://orcid.org/0000-0003-2460-9999
Vyacheslav N. Shalyapin https://orcid.org/0000-0003-3062-7835
Luis J. Goicoechea https://orcid.org/0000-0003-0110-834X
Scott E. Dahm https://orcid.org/0000-0002-2968-2418

References

Antonucci, R. 2013, Natur, 495, 165

```
Assef, R. J., Denney, K. D., Kochanek, C. S., et al. 2011, ApJ, 742, 93
Bate, N. F., Floyd, D. J. E., Webster, R. L., & Wyithe, J. S. B. 2008, MNRAS,
  391, 1955
Bate, N. F., Vernardos, G., O'Dowd, M. J., et al. 2018, MNRAS, 479, 4796
Bentz, M. C., Walsh, J. L., Barth, A. J., et al. 2010, ApJ, 716, 993
Bhatiani, S., Dai, X., & Guerras, E. 2019, ApJ, 885, 77
Birrer, S., Treu, T., Rusu, C. E., et al. 2019, MNRAS, 484, 4726
Blackburne, J. A., Pooley, D., Rappaport, S., & Schechter, P. L. 2011, ApJ,
  729, 34
Blaes, O. M. 2007, in ASP Conf. Ser. 373, The Central Engine of Active
   Galactic Nuclei, ed. L. C. Ho & J.-M. Wang (San Francisco, CA: ASP), 75
Bonning, E. W., Shields, G. A., Stevens, A. C., & Salviander, S. 2013, ApJ,
   770, 30
Bonvin, V., Courbin, F., Suyu, S. H., et al. 2017, MNRAS, 465, 4914
Boyle, B. J., & Terlevich, R. J. 1998, MNRAS, 293, L49
Cackett, E. M., Chiang, C.-Y., McHardy, I., et al. 2018, ApJ, 857, 53
Cackett, E. M., Horne, K., & Winkler, H. 2007, MNRAS, 380, 669
Calderone, G., Nicastro, L., Ghisellini, G., et al. 2017, MNRAS, 472, 4051
Chang, K., & Refsdal, S. 1979, Natur, 282, 561
Chartas, G., Krawczynski, H., Zalesky, L., et al. 2017, ApJ, 837, 26
Chen, G. C. F., Fassnacht, C. D., Suyu, S. H., et al. 2019, MNRAS, 490, 1743
Congdon, A. B., Keeton, C. R., & Osmer, S. J. 2007, MNRAS, 376, 263
Cornachione, M. A., & Morgan, C. W. 2020, ApJ, 895, 93
Cornachione, M. A., Morgan, C. W., Millon, M., et al. 2020, ApJ, 895, 125
Dai, X., Kochanek, C. S., Chartas, G., et al. 2010, ApJ, 709, 278
Dai, X., Steele, S., Guerras, E., Morgan, C. W., & Chen, B. 2019, ApJ, 879, 35
Davis, S. W., Woo, J.-H., & Blaes, O. M. 2007, ApJ, 668, 682
Di Matteo, T., Springel, V., & Hernquist, L. 2005, Natur, 433, 604
Edelson, R., Gelbord, J., Cackett, E., et al. 2019, ApJ, 870, 123
Edelson, R., Gelbord, J. M., Horne, K., et al. 2015, ApJ, 806, 129
Eigenbrod, A., Courbin, F., Meylan, G., et al. 2008, A&A, 490, 933
Eulaers, E., & Magain, P. 2011, A&A, 536, A44
Fabian, A. C., Iwasawa, K., Reynolds, C. S., & Young, A. J. 2000, PASP,
   112, 1145
Fadely, R., Keeton, C. R., Nakajima, R., & Bernstein, G. M. 2010, ApJ,
  711, 246
Fischer, J., Vrba, F. J., Toomey, D. W., et al. 2003, Proc. SPIE, 4841, 564
Floyd, D. J. E., Bate, N. F., & Webster, R. L. 2009, MNRAS, 398, 233
Foreman-Mackey, D., Agol, E., Ambikasaran, S., & Angus, R. 2017, AJ,
Gil-Merino, R., Goicoechea, L. J., Shalyapin, V. N., & Braga, V. F. 2012, ApJ,
Gil-Merino, R., Goicoechea, L. J., Shalyapin, V. N., & Oscoz, A. 2018, A&A,
   616, A118
Glikman, E., Helfand, D. J., & White, R. L. 2006, ApJ, 640, 579
Goicoechea, L. J., Artamonov, B. P., Shalyapin, V. N., et al. 2020, A&A,
Goicoechea, L. J., Shalyapin, V. N., Koptelova, E., et al. 2008, NewA, 13, 182
Gould, A. 2000, ApJ, 535, 928
Hainline, L. J., Morgan, C. W., Beach, J. N., et al. 2012, ApJ, 744, 104
Hainline, L. J., Morgan, C. W., MacLeod, C. L., et al. 2013, ApJ, 774, 69
Hernán-Caballero, A., Hatziminaoglou, E., Alonso-Herrero, A., & Mateos, S.
   2016, MNRAS, 463, 2064
Hinshaw, G., Weiland, J. L., Hill, R. S., et al. 2009, ApJS, 180, 225
Jiang, Y.-F., Davis, S. W., & Stone, J. M. 2016, ApJ, 827, 10
Jiménez-Vicente, J., Mediavilla, E., Kochanek, C. S., et al. 2014, ApJ, 783, 47
Jiménez-Vicente, J., Mediavilla, E., Muñoz, J. A., & Kochanek, C. S. 2012,
    ApJ, 751, 106
Kochanek, C. S. 2004, ApJ, 605, 58
Kochanek, C. S., Morgan, N. D., Falco, E. E., et al. 2006, ApJ, 640, 47
Lehár, J., Falco, E. E., Kochanek, C. S., et al. 2000, ApJ, 536, 584
LSST Science Collaboration, Abell, P. A., Allison, J., et al. 2009,
  arXiv:0912.0201
Lusso, E., & Risaliti, G. 2017, A&A, 602, A79
MacLeod, C. L., Morgan, C. W., Mosquera, A., et al. 2015, ApJ, 806, 258
McHardy, I. M., Cameron, D. T., Dwelly, T., et al. 2014, MNRAS, 444, 1469
McLeod, B. A., Bernstein, G. M., Rieke, M. J., & Weedman, D. W. 1998, AJ,
Mediavilla, E., Muñoz, J. A., Kochanek, C. S., et al. 2011, ApJ, 730, 16
Morgan, C. W., Hyer, G. E., Bonvin, V., et al. 2018, ApJ, 869, 106
Morgan, C. W., Kochanek, C. S., Dai, X., Morgan, N. D., & Falco, E. E. 2008,
   ApJ, 689, 755
```

```
Morgan, C. W., Kochanek, C. S., Morgan, N. D., & Falco, E. E. 2010, ApJ,
  712, 1129
Mortonson, M. J., Schechter, P. L., & Wambsganss, J. 2005, ApJ, 628, 594
Mosquera, A. M., & Kochanek, C. S. 2011, ApJ, 738, 96
Motta, V., Mediavilla, E., Falco, E., & Muñoz, J. A. 2012, ApJ, 755, 82
Motta, V., Mediavilla, E., Rojas, K., et al. 2017, ApJ, 835, 132
Mróz, P., Udalski, A., Skowron, J., et al. 2017, Natur, 548, 183
Muñoz, J. A., Vives-Arias, H., Mosquera, A. M., et al. 2016, ApJ, 817, 155
Navarro, J. F., Frenk, C. S., & White, S. D. M. 1997, ApJ, 490, 493
Peterson, B. M., Ferrarese, L., Gilbert, K. M., et al. 2004, ApJ, 613, 682
Poindexter, S., & Kochanek, C. S. 2010, ApJ, 712, 658
Poindexter, S., Morgan, N., & Kochanek, C. S. 2008, ApJ, 673, 34
Pooley, D., Anguita, T., Bhatiani, S., et al. 2019, BAAS, 51, 411
Pooley, D., Blackburne, J. A., Rappaport, S., & Schechter, P. L. 2007, ApJ,
  661, 19
Refsdal, S., Stabell, R., Pelt, J., & Schild, R. 2000, A&A, 360, 10
Rojas, K., Motta, V., Mediavilla, E., et al. 2014, ApJ, 797, 61
Rojas, K., Motta, V., Mediavilla, E., et al. 2020, ApJ, 890, 3
Schechter, P. L., & Wambsganss, J. 2002, ApJ, 580, 685
```

```
Shajib, A. J., Birrer, S., Treu, T., et al. 2019, MNRAS, 483, 5649
Shakura, N. I., & Sunyaev, R. A. 1973, A&A, 500, 33
Shalyapin, V. N., Goicoechea, L. J., & Gil-Merino, R. 2012, A&A, 540,
  A132
Shalyapin, V. N., Goicoechea, L. J., Koptelova, E., Ullán, A., & Gil-Merino, R.
  2008, A&A, 492, 401
Shen, Y. 2016, ApJ, 817, 55
Sluse, D., Chantry, V., Magain, P., Courbin, F., & Meylan, G. 2012, A&A,
  538, A99
Steele, I. A., Smith, R. J., Rees, P. C., et al. 2004, Proc. SPIE, 5489, 679
Suyu, S. H., Auger, M. W., Hilbert, S., et al. 2013, ApJ, 766, 70
Tewes, M., Courbin, F., & Meylan, G. 2013, A&A, 553, A120
van Dokkum, P. G. 2001, PASP, 113, 1420
Vanden Berk, D. E., Richards, G. T., Bauer, A., et al. 2001, AJ, 122, 549
Walsh, D., Carswell, R. F., & Weymann, R. J. 1979, Natur, 279, 381
Watson, D., Denney, K. D., Vestergaard, M., & Davis, T. M. 2011, ApJL,
  740, L49
Wong, K. C., Suyu, S. H., Chen, G. C. F., et al. 2020, MNRAS, 498, 1420
Xie, X., Shao, Z., Shen, S., Liu, H., & Li, L. 2016, ApJ, 824, 38
```